IOPscience iopscience.iop.org

Home Search Collections Journals About Contact us My IOPscience

Parasitic coupling in magneto-inductive cable

This content has been downloaded from IOPscience. Please scroll down to see the full text.

2017 J. Phys. D: Appl. Phys. 50 225001

(http://iopscience.iop.org/0022-3727/50/22/225001)

View the table of contents for this issue, or go to the journal homepage for more

Download details:

IP Address: 155.198.134.54
This content was downloaded on 30/06/2017 at 15:21

Please note that terms and conditions apply.

You may also be interested in:

Thin-film magneto-inductive cables
R R A Syms, L Solymar, I R Young et al.

Broadband coupling transducers for magneto-inductive cables
R R A Syms, L Solymar and I R Young

Low-loss magneto-inductive waveguides
R R A Syms, I R Young and L Solymar

MI waves supported by metamaterial elements
E Shamonina and L Solymar

Left-handed metamaterial using Z-shaped SRR for multiband application by azimuthal angular rotations
Md Mehedi Hasan and Mohammad Rashed Iqbal Faruque

Tunable superconducting nanoinductors
Anthony J Annunziata, Daniel F Santavicca, Luigi Frunzio et al.

Micromachined high-performance RF passives in CMOS substrate
Xinxin Li, Zao Ni, Lei Gu et al.

Analysis of resonant planar dissipative network antennas for rf inductively coupled plasma sources
Ph Guittienne, A A Howling and Ch Hollenstein

Parametric amplification in coupled magnetoinductive waveguides
O Sydoruk, E Shamonina and L Solymar

IOP Publishing Journal of Physics D: Applied Physics
J. Phys. D: Appl. Phys. **50** (2017) 225001 (9pp) https://doi.org/10.1088/1361-6463/aa6d06

Parasitic coupling in magneto-inductive cable

Richard R A Syms[1,3] **and Timmy Floume**[2]

[1] EEE Department, Imperial College London, Exhibition Road, London SW7 2AZ, United Kingdom
[2] GreenerWave, Institut Langevin, 1 Rue Jussieu, 75005 Paris, France

E-mail: r.syms@imperial.ac.uk and timmy@floume.com

Received 9 February 2017, revised 9 April 2017
Accepted for publication 12 April 2017
Published 11 May 2017

Abstract

Magneto-inductive (MI) waveguides are linear arrangements of magnetically coupled *L–C* resonators that propagate electrical energy at radio frequency without direct connection. To achieve the strong magnetic coupling needed for low-loss propagation, adjacent elements must be in such close proximity that electric coupling arises. In contrast to electric coupling in split ring resonators, the coupling occurs between the inductive tracks of adjacent resonant loops. Parasitic capacitance is demonstrated in flexible magneto-inductive cable, and shown to introduce additional propagation bands above the MI band. Simple models are developed to predict this effect, and strategies discussed to improve high-frequency isolation.

Keywords: metamaterial, magneto-inductive waveguide, parasitic

(Some figures may appear in colour only in the online journal)

1. Introduction

Since the 1940s, there has been considerable interest in periodic arrangements of small numbers of coupled *L–C* networks for use as filters [1–3]. The coupling can be electric or magnetic, with the former generally providing the best performance. However, magnetically coupled systems have still attracted attention as band-pass filters, and designs have been optimized to yield a given response even in the presence of loss [4–7]. Interest has continued to modern times [8].

More recently, current waves propagating in larger periodic arrangements of magnetically coupled *L–C* resonators have been re-christened 'magnetoinductive' (MI) waves [9–11]. Such waves have been observed in many magnetically coupled systems [12–15], and applications have been proposed for 1D and 2D systems in communications [16–21], power transfer [22–26] and sensing [27, 28], particularly for magnetic resonance imaging (MRI) [29–33]. However, since the losses in MI systems are much higher those of conventional solutions such as coaxial cables, particular circumstances are required to justify their use. In communications and power transfer these include the ability to transfer energy through free space and dielectric walls. In internal MRI, these include the enhancement to patient safety that follows from segmentation, since this eliminates extended linear conductors on which common-mode standing waves may be excited by the electric field of the scanner's powerful transmitter.

Propagation loss is minimized at the resonant frequency, when group velocity is at its highest, and high performance requires large quality factors and strong magnetic coupling. MI cables have been developed to obtain large propagation distances from a limited number of resonant elements, in a flexible format compatible with probes for internal MRI [33]. The element design (which uses two capacitors, rather than one) allows printing of cables without the need for via connections [34]. It also allows the formation of a simple resonant transducer from a halved element, which can provide exact matching to real impedance at two different frequencies, and improved matching between [35]. The use of identical elements prevents the local optimization used to control pass-band shape in filters, but this is relatively unimportant for narrow-band applications such as MRI. To achieve immunity to bending, the element shape is long and thin, and adjacent elements are strongly overlapped [36]. However, the price is an increase in parasitic effects compared with filters based on square elements on rigid substrates.

It is generally assumed that the coupling in MI systems is exclusively magnetic. However, the possibility of additional

[3] Author to whom any correspondence should be addressed.

 © 2017 IOP Publishing Ltd Printed in the UK

electric coupling has been investigated in studies of planar-coupled microwave split ring resonators (SRRs) [37, 38], and exploited in arrangements with alternating types of coupling [39]. The coupling was attributed to an inhomogeneous charge distribution in the SRR gap region, resulting in a high electric field that can modify the charge in adjacent elements. However, for sufficiently high magnetic coupling, the tracks of adjacent elements in a magneto-inductive cable must be close together, this time resulting in electric coupling between the inductors. A preliminary discussion of this effect was presented in [40]. The aim here is to present a complete description, and show that it represents a significant and unavoidable non-ideality. In section 2, we demonstrate strongly coupled cables, and show they exhibit parasitic pass-bands above the MI band that cannot be explained by conventional theory. In section 3, we consider the physical basis for electric coupling. In section 4, we develop equivalent circuit models capable of explaining the observed response. Conclusions are presented in section 5.

2. Magneto-inductive cable

Magneto-inductive cable is a high performance form of MI waveguide [34]. Each loop is formed from printed copper inductors on a thin, flexible substrate, together with printed or surface mount capacitors. Figure 1(a) shows a plan view near a single element. The loops are divided into two halves, each of inductance $L/2$. The capacitors are also divided into two, each of value $2C$. Figure 1(b) shows a section view. Alternate loops are formed on either side of a substrate and overlaid with a lateral offset of one conductor width. High nearest neighbour magnetic coupling is then obtained, while non-nearest neighbour coupling is negligible. Despite the planar layout, the arrangement leads to axial coupling, with a positive magnetic coupling coefficient [9]. Figure 1(c) shows an approximation to the cross-sectional arrangement, which will be discussed later.

Experimental cables have been constructed from copper-clad Kapton® HN (Dupont High Performance Films). Inductors measuring 66 mm × 5 mm were formed with a track width of 0.5 mm and a thickness of 35 μm on a dielectric of thickness 25 μm and arranged with a period $a = 35$ mm. The printed circuit board contained arrays of cables, together with single and paired elements used to extract circuit parameters. Figure 2 shows a panel of elements and a completed cable. Surface mount capacitors were added in the locations shown to tune the resonance to the frequency for which the mid-band impedance $Z_{0M} = \omega_0 M$ (see below) equalled 50 Ω. Broadband transducers (which provide impedance matching at two frequencies [35]) were constructed from halved elements and SMA connectors. Ten elements and two transducers were overlaid to form a cable 385 mm long.

Parameters were estimated using inductive probes and a network analyzer. The self-inductance L and Q-factor were found by measuring the resonant frequency $f_0 = 1/[2\pi\sqrt{(LC)}] = 227.5$ MHz and half-power bandwidth of a single element with known capacitance $C = 4.7$ pF, as shown in figure 3. The mutual inductance M and coupling coefficient $\kappa = 2\ M/L$ were found from the split resonant frequencies $f_{1,2} = 1/[2\pi\sqrt{\{(L \pm M)C\}}]$ of a coupled pair, namely $f_1 = 201.6$ MHz and $f_2 = 280.8$ MHz. The following values were obtained: $L = 104$ nH, $Q = 110$, $M = 34.4$ nH and $\kappa = 0.66$. The frequency giving $Z_{0M} = 50\ \Omega$ was estimated from the values of $\omega_0 = 2\pi f_0$ and M as 231.5 MHz, which required $C = 4.55$ pF. As described earlier, the closest available value ($C = 4.7$ pF) was used, reducing f_0 slightly. However, unexplained high frequency resonances were noted in the mode spectrum. One is shown at $f_3 = 1.08$ GHz; the next, less distinct resonance lay at $f_4 \approx 3.3$ GHz.

Transmission was also measured using the network analyzer, with the cable in a U-shape between the measurement ports. The full line in figure 4 shows the frequency variation of S_{21} up to 3 GHz. The MI band extends over the frequency range 200–400 MHz. The minimum insertion loss is 2.2 dB, corresponding to a propagation loss of ≈5.7 dB m^{-1}. However, there is also propagation a much wider band between 750 MHz and 2.5 GHz, where there are multiple resonances due to standing waves. Clearly, the effect is associated with the additional resonance at f_3, but despite its wide spacing from f_0 the parasitic band extends very close to the MI band. We have noted similar phenomena in seven cable designs with centre frequencies ranging from 20–300 MHz. In fact, a second parasitic band was visible in all such cables. Higher bands were visible in some cables, but their existence was often masked by increased loss at high frequency

The measurements were compared with standard theory [9] as follows. Figure 5 shows a link consisting of N resonant elements between a source and a load. Ignoring loss, non-nearest neighbour coupling and other parasitic effects, the current I_n in the nth element of the periodic section at angular frequency ω is related to the currents I_{n-1} and I_{n+1} by the recursion equation:

$$\left(j\omega L + \frac{1}{j\omega C}\right) I_n + j\omega M(I_{n-1} + I_{n+1}) = 0. \tag{1}$$

Assumption of the travelling wave solution $I_n = I_0 \exp(-jnka)$, where k is the propagation constant and a is the period, then leads to the dispersion equation [10]:

$$\cos(ka) = -\left(1 - \frac{\omega_0^2}{\omega^2}\right)/\kappa. \tag{2}$$

Here $\omega_0 = 1/\sqrt{(LC)}$ is the angular resonant frequency and $\kappa = 2\ M/L$. In the lossless case, propagation is band-limited. Resistive loss R in the inductor may be incorporated, by replacing $j\omega L$ with $j\omega L(1 - j\omega_0/\omega Q)$, where $Q = \omega_0 L/R$ is the quality factor of the elements. Its effect is to render k complex (so that $k = k' - jk''$), introduce propagation loss and allow out-of-band propagation. For low loss, k' is approximately as in the lossless case, while $k'' \approx 1/\{\kappa Q \sin(k'a)\}$. At resonance, $k'' \approx 1/\kappa Q$, so that strong coupling and a high Q-factor are required for low loss.

The first element is excited using a source with output impedance Z_0 and voltage V_1, while the last is terminated using the same impedance. The characteristic impedance of a MI

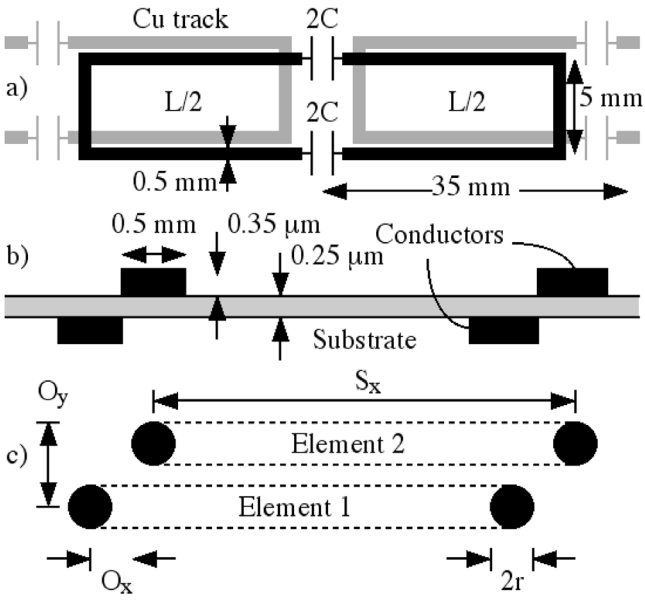

Figure 1. (a) Plan and (b) section view of MI cable; (c) approximate cross-sectional geometry. © 2013 IEEE. Reprinted, with permission, from [40].

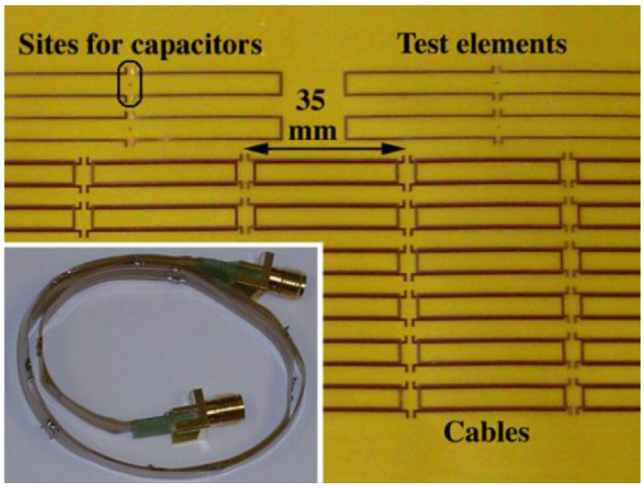

Figure 2. Kapton PCB and completed magneto-inductive cable. © 2013 IEEE. Reprinted, with permission, from [40].

waveguide is $j\omega M\exp(-jka)$ [11]. At resonance, this expression reduces to the real value $Z_{0M} = \omega_0 M$. If Z_{0M} matches Z_0, there will then be no reflections. However, broadband transducers allow a considerable improvement in performance, since they provide an exact impedance match at two frequencies [35]. Their implementation merely requires the inductance of the terminating elements to be halved and their capacitance doubled, as shown in figure 5. Ignoring line losses again, Kirchhoff's voltage law then gives for the first and last element:

$$\left(\frac{j\omega L}{2} + \frac{1}{2j\omega C} + Z_0\right)I_1 + j\omega M I_2 = V_1$$
$$\left(\frac{j\omega L}{2} + \frac{1}{2j\omega C} + Z_0\right)I_N + j\omega M I_{N-1} = 0. \qquad (3)$$

Equations (1) and (3) form a set of N equations that may be written in a matrix form as $Z\,I = V$. Here Z is an $N \times N$ impedance matrix while I and V are N-element vectors of currents and voltages. Only the first element of V is non-zero, and given by V_1. The currents I_n can be found by inverting the matrix equation, and the transmission scattering parameter S_{21} extracted by standard methods. The dotted line in figure 4 compares the predictions of this theory with the previous experimental results, assuming $N = 12$ to correspond to a 10-element line with 2 transducers. There is good agreement within the MI band, but the theory cannot explain the propagation at high frequency.

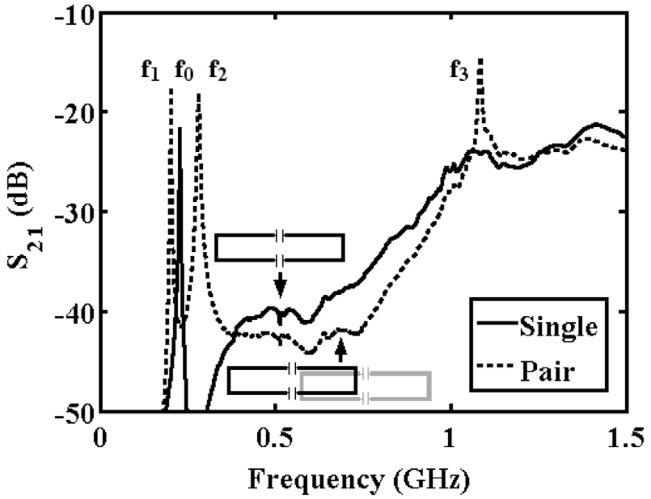

Figure 3. Resonance spectra for a single resonant element and a coupled pair.

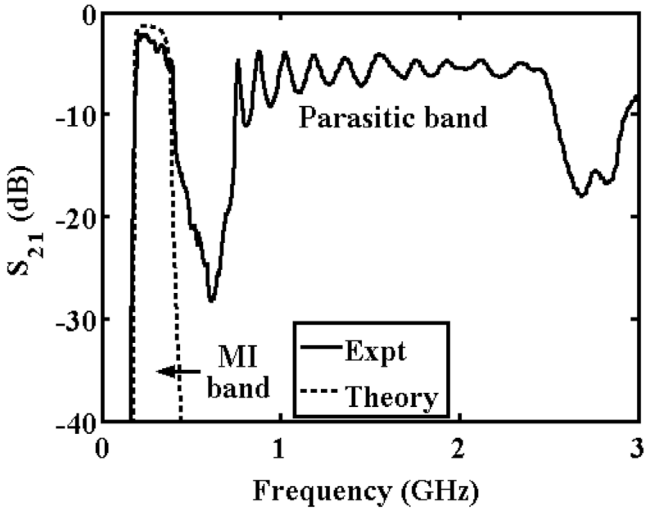

Figure 4. Comparison of the experimental frequency variation of S_{21} and the predictions of the standard magneto-inductive model.

3. Parasitic electric coupling

We now develop a model to explain the observed effects. Estimation of equivalent circuit parameters can be extremely complicated for rectangular loops and rectangular wires. We therefore use an approximation based on infinite, parallel cylindrical wires, which yields analytic results easily. In this model, the cable cross-section in the overlap region is as shown in figure 1(c). Here, two elements based on wires of

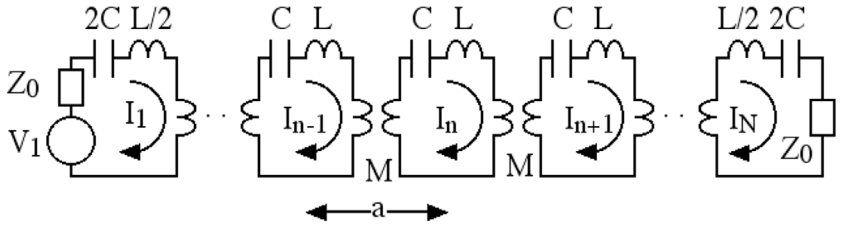

Figure 5. Equivalent circuit of a point-to-point magneto-inductive link. © 2013 IEEE. Reprinted, with permission, from [40].

radius r and separation S_x overlap with offsets O_x and O_y in the two perpendicular directions. Ignoring the ends of the loops, the per-unit-length self inductance L_{PUL} and the mutual inductance M_{PUL} between elements can be found by calculating the magnetic flux due to currents in a first pair of wires and integrating the perpendicular component of flux passing through the first or second pair, respectively. The results are:

$$L_{\mathrm{PUL}} = (\mu_0/\pi)\log_e\{(S_x - r)/r\} \tag{4}$$

$$\begin{aligned} M_{\mathrm{PUL}} &= (\mu_0/4\pi)\log_e\{A/B\} \text{ with} \\ A &= \{(O_x + S_x - r)^2 + O_y^2\}\ \{(O_x - S_x + r)^2 + O_y^2\} \\ B &= \{(O_x + r)^2 + O_y^2\}\ \{(O_x - r)^2 + O_y^2\}. \end{aligned} \tag{5}$$

However, it is well known that significant capacitance exists between closely spaced cylindrical conductors. The per-unit-length capacitance C_{PUL} between the closest wires can again be found by calculating the total electric field due to line charges on a pair of wires with centres chosen to yield equipotentials co-located with the real wires, and integrating this field to find the voltage between the real wires. The result is:

$$\begin{aligned} C_{\mathrm{PUL}} &= (\pi\varepsilon_0)/\log_e\left\{\frac{d}{2a} + \sqrt{\left(\frac{d^2}{4r^2} - 1\right)}\right\} \\ &\text{with } d = \sqrt{(O_x^2 + O_y^2)}. \end{aligned} \tag{6}$$

Unfortunately, since L_{PUL}, M_{PUL} and C_{PUL} all depend on the geometric constants r, S_x, O_x and O_y, it is difficult to obtain high values of the first two without the third also being high. For the high-frequency cable of the previous section, this model suggests equivalent circuit parameters $L \approx a' L_{\mathrm{PUL}}$ and $M \approx a'' M_{\mathrm{PUL}}$ where $a' = 66$ mm is the inductor length and $a'' = 31$ mm is the overlap length. Assuming an equivalent conductor radius $r = 225$ μm (slightly reduced from the value of 250 μm suggested by the track width), a conductor separation $S_x = 5$ mm, and offsets of $O_x = 0.5$ mm and $O_y = (25 + 37.5) = 62.5$ μm yields $L = 80.7$ nH, $M = 29.1$ nH and $\kappa = 0.72$. These values are broadly in agreement with measurements (104 nH, 34.4 nH, and 0.66, respectively), but there are discrepancies attributable to the approximations made to the inductor and track shapes. An alternative and possibly more realistic model might be constructed using filamentary currents, as was done in [31]. More importantly, the model implies a parasitic capacitance $C_{\mathrm{P}} \approx 2a'' C_{\mathrm{PUL}} = 3.6$ pF between elements, comparable to the value $C = 4.7$ pF used to achieve resonance.

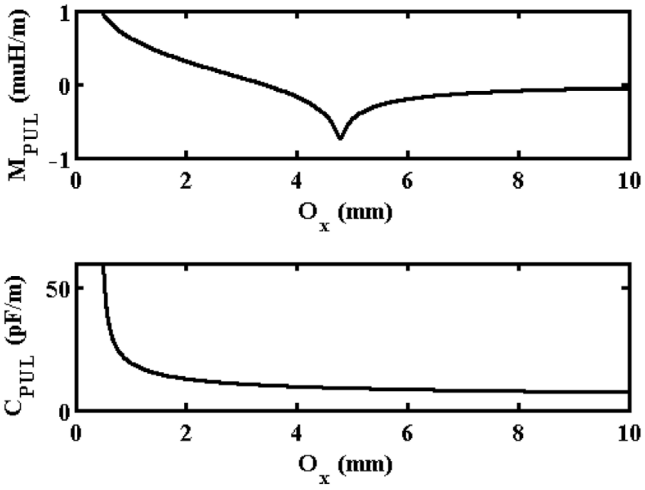

Figure 6. Variation of per-unit-length circuit parameters M_{PUL} and C_{PUL} with lateral offset O_x, for $r = 225$ μm, $S_x = 5$ mm and $O_y = 62.5$ μm.

There is limited scope to improve matters. Figure 6 shows the variation of M_{PUL} and C_{PUL} with O_x, assuming that $r = 225$ μm, $S_x = 5$ mm and $O_y = 62.5$ μm. Both fall as O_x increases. M_{PUL} is positive when $O_x/S_x = 0$, but falls to zero when $O_x/S_x \approx 1/\sqrt{2}$ and becomes negative as the geometry alters from axial to planar. C_{PUL} falls monotonically, and initially rather faster. Importantly, if S_x is increased, the variation of M_{PUL} approximately scales, while the variation of C_{PUL} stays unchanged. These characteristics imply that it should be possible to reduce C_{P} by increasing O_x. However, additional loss will then be caused by the accompanying reduction in M. Similar effects follow from a reduction in the axial overlap of adjacent elements. An alternative strategy would be to leave the geometry unaltered, but reduce the resonant frequency by increasing C. This approach will space the MI band further from the spurious pass-band. However, additional loss will again arise, this time from the reduction in Q-factor. Thus, it appears that there are intrinsic limits to the performance of MI cables.

4. Equivalent circuit models

We now develop equivalent circuit models capable of simulating the measured response. Figure 7(a) shows the simplest possibility. One complete element is shown, together with parts of near neighbours. Electric coupling is represented using discrete capacitors shunting the tracks of adjacent elements. Here we use two capacitors $C_{\mathrm{P}}/4$ connecting the extremities of each pair of tracks. The total inductance

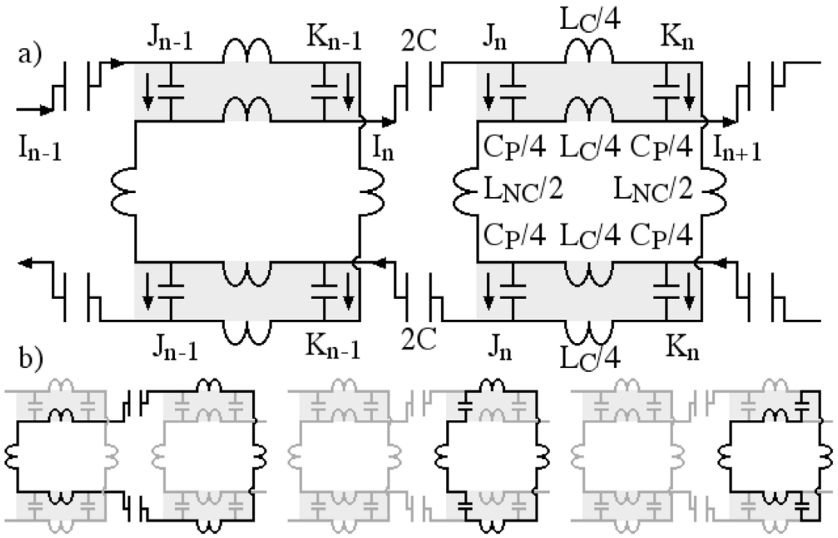

Figure 7. (a) Equivalent circuit of MI cable, including two parasitic capacitors for each coupled track section; (b) closed loops used to develop circuit equations. © 2013 IEEE. Reprinted, with permission, from [40].

is therefore split into six parts. Four inductances $L_C/4$ correspond to the four horizontal track sections while two others $L_{NC}/2$ such that $L_C + L_{NC} = L$ correspond to the two vertical sections. For simplicity, we assume that magnetic coupling only takes place between the inductors $L_C/4$. This approximation avoids the need to consider magnetic fields in detail, but still generates realistic results. Consequently, there is a mutual inductance $M/2$ in each shaded region.

For a periodic line, we need only consider two currents J_n and K_n in the parasitic capacitors in addition to the main current I_n. Use of Kirchhoff's voltage law around the three loops in figure 7(b) gives three equations relating the currents. Once again, we ignore losses, since they can be included later by modifying impedances. For the resonator loop itself we obtain:

$$(j\omega L + 1/j\omega C)I_n + j\omega M(I_{n-1} + I_{n+1}) - j\omega\left(\frac{L_{NC}}{2} + M\right)(J_{n-1} + K_n) - j\left(\frac{\omega L}{2}\right)(J_n + K_{n-1}) = 0. \quad (7)$$

Similarly, for two loops including parasitic capacitors we get:

$$j\left(\frac{\omega L}{2}\right)I_n + j\omega\left(\frac{L_{NC}}{2} + M\right)I_{n+1} - \left(\frac{j\omega(L_C + 2L_{NC})}{2} + \frac{8}{j\omega C_P}\right)J_n - j\omega(L_{NC} + M)K_n = 0$$

$$j\omega\left(\frac{L_{NC}}{2} + M\right)I_n + j\left(\frac{\omega L}{2}\right)I_{n+1} - j\omega(L_{NC} + M)J_n - \left(\frac{j\omega(L_C + 2L_{NC})}{2} + \frac{8}{j\omega C_P}\right)K_n = 0. \quad (8)$$

Assumption of the travelling wave solutions $I_n = I_0 \exp(-jnka)$, $J_n = J_0 \exp(-jnka)$ and $K_n = K_0 \exp(-jnka)$ again allows a dispersion equation to be derived. The manipulations are relatively lengthy, and will not be detailed here; however, the result is:

$$\cos(ka) = -f_1/f_2 \text{ with}$$

$$f_1 = (1 - \omega_0^2/\omega^2)\left\{\left(a_1 - \frac{a_4^2\omega_0^2}{\omega^2}\right)^2 - a_2^2\right\} - \frac{(1 + a_3^2)\left(a_1 - \frac{a_4^2\omega_0^2}{\omega^2}\right)}{2} + a_2a_3$$

$$f_2 = \kappa\left\{\left(a_1 - \frac{a_4^2\omega_0^2}{\omega^2}\right)^2 - a_2^2\right\} - a_3\left(a_1 - \frac{a_4^2\omega_0^2}{\omega^2}\right) + a_2(1 + a_3^2)/2$$

$$a_1 = \frac{(1 + \alpha)}{2};$$

$$a_2 = \alpha + \frac{\kappa}{2}; a_3 = \alpha + \kappa;\ a_4 = \frac{\omega_{0P}}{\omega_0};$$

$$\alpha = \frac{L_{NC}}{L};\ \omega_{0P} = \sqrt{(8/LC_P)}. \quad (9)$$

The model has therefore introduced two new parameters, α (which depends on the geometric arrangement of the inductors) and ω_{0P} (which depends on the parasitic capacitance C_P). However, when C_P is small, ω_{0P} and a_4 are large, and we recover the MI dispersion equation near $\omega = \omega_0$.

Figure 8 shows dispersion characteristics calculated assuming the previous experimental parameters ($f_0 = 227.5$ MHz, $\kappa = 0.66$) and a value of α obtained from the track lengths defining L_C and L_{NC}, namely, $5/(66 + 5) = 0.07$. The parasitic capacitance has been assumed as $C_P = 4.3$ pF for agreement with experimental results. Five characteristics are presented. The simplest model (with no parasitic capacitors) uses equation (2). In this case, there is only one branch in the dispersion diagram. The next simplest (with two parasitic capacitors per track section) uses equation (9). Three branches may now be seen: a MI branch at low frequency, and two new branches at higher frequency. The MI branch is almost identical to the prediction of the simple model, and supports forward waves. In contrast, the first parasitic branch supports backward waves. Increasing C_P forces it closer to the

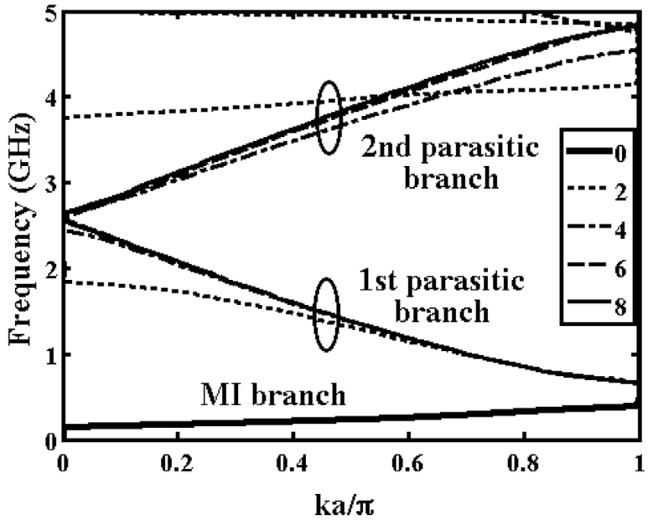

Figure 8. Dispersion diagrams for MI cable with 0, 2, 4, 6 and 8 parasitic capacitors per coupled track section, with parameters corresponding to the experiment.

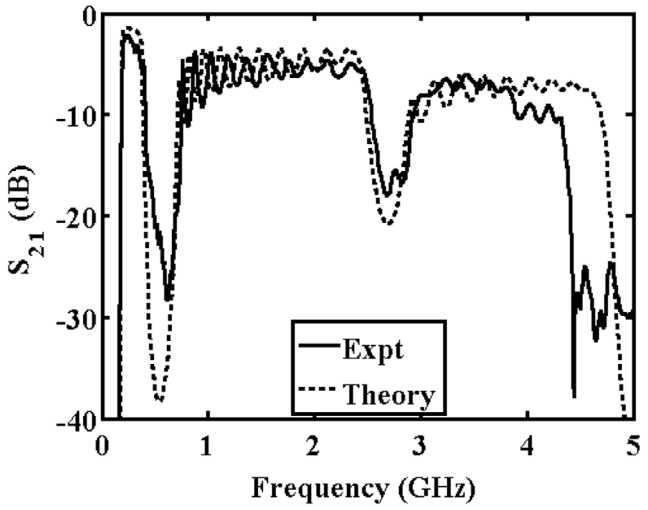

Figure 9. Comparison of the experimental frequency variation of S_{21} with the predictions of the new model with 16 parasitic capacitors per coupled track section.

MI branch, while increasing α mainly alters the separation between the first and second parasitic branches.

These findings are at least qualitatively correct. However, the circuit of figure 7(a) is an extreme simplification. More realistically, the self-inductance, mutual inductance and parasitic capacitance must all be distributed. We have therefore developed more detailed models in which the parasitic capacitance $C_P/2$ of each pair of tracks is separated into N_C elements distributed along the shaded regions, and the corresponding self- and mutual inductance $L_C/4$ and $M/2$ are subdivided into $N_C - 1$ elements. The currents may then vary in position for $N_C > 2$. We have investigated models up to $N_C = 16$. Although simple to construct, the recurrence equations are tedious. We therefore present only the equations for $N_C = 4$, detailed in Appendix.

By making travelling wave substitutions, these equations may be converted into coupled dispersion relations, which may then be solved numerically. The three additional characteristics in figure 8 shows the predictions of these more

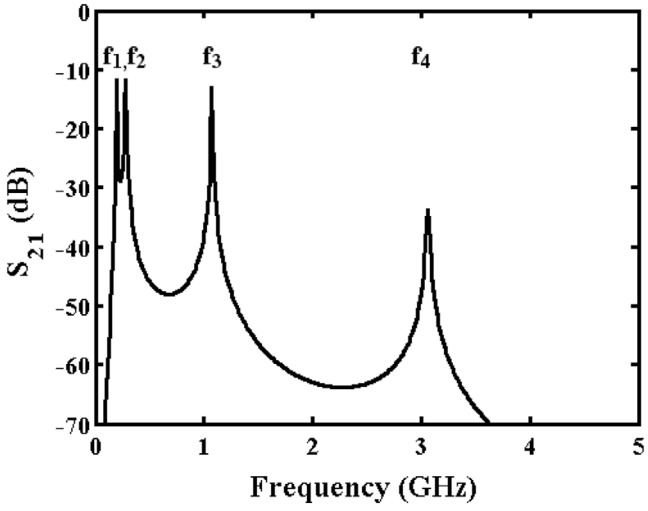

Figure 10. Theoretically predicted mode spectrum of coupled element pair.

complicated models, assuming $N_C = 4$, 6 and 8, respectively. The effect of the subdivision is to modify the diagram still further. For example, as N_C rises, the ranges of the lower parasitic bands alter. There are large discrepancies between the bandwidths predicted with $N_C = 2$ and $N_C = 4$; however there is steady convergence, and little difference between results with $N_C = 6$ and $N_C = 8$. For example, the upper edge of the second parasitic branch is predicted to lie at 4.11, 4.77, 4.81 and 4.81 GHz by models with $N_C = 2$, 4, 6 and 8, respectively. The number of bands also alters, and at high frequency every increment in N_C inserts an additional band (not shown). Importantly, the first parasitic band lies close to the MI band, and has a much larger bandwidth.

Similar models may be used to simulate end-to-end transmission in a line. However, the equations must be modified at the input and output transducers, to account for the different local circuit in these loops. For an N-element line, a total of $(N_C + 1)N - N_C$ circuit equations must therefore be constructed. Although cumbersome, the matrix Z is simple to define, since the impedance values follow a regular pattern. Matrix inversion may then be used to calculate the current I_N and the power transmission coefficient. Loss must also be considered. Here we have ignored loss in the surface mount capacitors, focusing on the higher loss expected in the inductors and parasitics. These are estimated as follows. At low frequency, the inductors have resistance R. At high frequency the skin effect will increase resistance to $Rt/2\delta$, where t is the conductor thickness, $\delta = \sqrt{(2/\omega\mu_0\sigma)}$ is the skin depth in a material of conductivity $\sigma(5.8 \times 10^7$ S m^{-1} for copper), and $\mu_0 = 4\pi \times 10^{-7}$ H m^{-1} is the permeability of free space. The parasitic capacitance involves electric fields that exist partly in air and partly in the substrate. We have included dielectric loss by writing this term as $C_P\{1 - j\tan(\delta)\}$, where $\tan(\delta)$ is an effective loss tangent.

The dotted line in figure 9 shows a comparison between the earlier experimental data and this model, assuming the previous parameters and $\tan(\delta) = 0.012$, $N_C = 16$. Here the frequency range is extended to include the second parasitic band. The lowest parasitic band is correctly predicted, as are the peaks and troughs due to standing waves. The agreement between experiment and theory is worse for the second band. The most

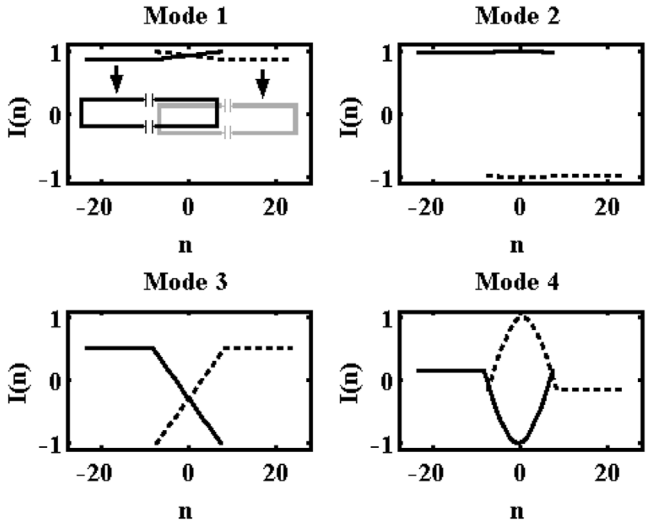

Figure 11. Theoretical current variations along the tracks of coupled elements, at the first four resonances.

likely explanations are the capacitance between the inductor tracks of the same element (which leads to self-resonance) and radiation, both of which are neglected. In other measurements (not shown) we have observed as many as four parasitic bands over a wider frequency range, in qualitative agreement with the model. However, losses are much higher, and both the data and the quantitative agreement appear less reliable.

The same theory can be used to predict the resonances of coupled elements. Rather than simulate the details of excitation, we have simply assumed a voltage source with 1 Ω output impedance at the extremity of one element and a similar load at the extremity of the other. Figure 10 shows the resonance spectrum thus obtained. The three resonances at f_1, f_2 and f_3 are correctly predicted. However, the resonance f_4 at 3 GHz is low by comparison with experiment (3.3 GHz). We believe this discrepancy to be due to further parasitic capacitance between the elements and the measurement probe itself. Figure 11 shows the normalised currents along the long conductors at the four frequencies. Here the index n is a normalised position, which (since each coupled track is divided into 16 sections) ranges from ≈ -24 to $+24$. Mode 1 (occurring at f_1) is the symmetric resonance of a pair of coupled *L–C* resonators. With no parasitic capacitance, the currents should be uniform and equal. Similarly, Mode 2 (at f_2) is the corresponding anti-symmetric resonance, and the currents should be equal and opposite. To a reasonable approximation, both distributions are as expected. Modes 3 and 4 are new symmetric and anti-symmetric resonances arising from the parasitic capacitance. In each case, large variations in the currents can be seen in the coupled track sections.

5. Conclusions

We have shown that strongly coupled magneto-inductive cable suffers from parasitic electric coupling, which introduces additional pass-bands that degrade isolation at high frequency. The mechanism is different from an apparently similar electric coupling noted in SRRs, since it involves coupling between the inductor tracks. Furthermore, since it is indivisibly linked with magnetic coupling, it is much more significant. The effects cannot be described using the standard model of magneto-inductive propagation. However, the addition of distributed parasitic capacitance to the equivalent circuit provides an excellent explanation. The model ignores self-resonance and radiation. Both are likely to modify the response further at high frequency. However, since the main interest of designers is likely to be at frequencies close to the MI band, the first parasitic band will be most important, and in this range the model appears realistic. If the electric coupling is relatively small, this band will lie above the MI band. However, if the electric coupling is much higher—which might occur, for example, if the tracks of adjacent elements are exactly overlaid—the two may merge. Since there appears to be no method of avoiding electric coupling, care should therefore be taken in designing strongly coupled MI cables to ensure a suitable balance between transmission efficiency and out-of-band signal rejection.

Appendix

If four parasitic capacitors are allowed per coupled track section, the equivalent circuit is as shown in figure A1(a). The circuit equations for the five loops in figure A1(b) are then as follows:

A.1. Main loop

$$\begin{aligned} &j\omega MI_{n-1} + \left\{j\omega(L_C + L_{NC}) + \frac{1}{j\omega C}\right\}I_n + j\omega MI_{n+1} \\ &-j\omega\left(\frac{L_{NC}}{2} + M\right)J_{n-1} - j\omega\left(\frac{L_C}{2} + \frac{L_{NC}}{2}\right)J_n \\ &-j\omega\left(\frac{L_C}{6} + \frac{L_{NC}}{2} + \frac{2M}{3}\right)K_{n-1} - j\omega\left(\frac{L_C}{3} + \frac{L_{NC}}{2} + \frac{M}{3}\right)K_n \\ &-j\omega\left(\frac{L_C}{3} + \frac{L_{NC}}{2} + \frac{M}{3}\right)L_{n-1} - j\omega\left(\frac{L_C}{6} + \frac{L_{NC}}{2} + \frac{2M}{3}\right)L_n \\ &-j\omega\left(\frac{L_C}{2} + \frac{L_{NC}}{2}\right)M_{n-1} - j\omega\left(\frac{L_{NC}}{2} + M\right)M_n = 0. \end{aligned} \tag{A.1}$$

A.2. Parasitic loop 1

$$\begin{aligned} &j\omega\left(\frac{L_C}{2} + \frac{L_{NC}}{2}\right)I_n + j\omega\left(\frac{L_{NC}}{2} + M\right)I_{n+1} \\ &-\left\{j\omega\left(\frac{L_C}{2} + L_{NC}\right) + \frac{16}{j\omega C_P}\right\}J_n \\ &-j\omega\left(\frac{L_C}{3} + L_{NC} + \frac{M}{3}\right)K_n \\ &-j\omega\left(\frac{L_C}{6} + L_{NC} + \frac{2M}{3}\right)L_n \\ &-j\omega(L_{NC} + M)M_n = 0. \end{aligned} \tag{A.2}$$

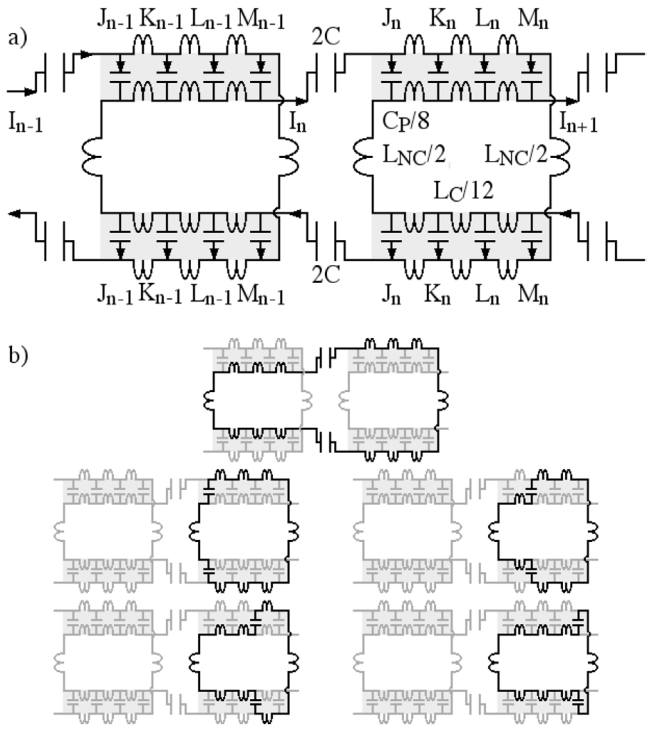

Figure A1. (a) Equivalent circuit of MI cable, including four parasitic capacitors for each coupled track section; (b) closed loops used to develop circuit equations.

A.3. Parasitic loop 2

$$
\begin{aligned}
&j\omega\left(\frac{L_C}{3}+\frac{L_{NC}}{2}+\frac{M}{3}\right)I_n+j\omega\left(\frac{L_C}{6}+\frac{L_{NC}}{2}+\frac{2M}{3}\right)I_{n+1}\\
&-j\omega\left(\frac{L_C}{3}+L_{NC}+\frac{M}{3}\right)J_n\\
&-\left\{j\omega\left(\frac{L_C}{2}+L_{NC}\right)+\frac{16}{j\omega C_P}\right\}K_n\\
&-j\omega\left(\frac{L_C}{3}+L_{NC}+\frac{M}{3}\right)L_n\\
&-j\omega\left(\frac{L_C}{6}+L_{NC}+\frac{2M}{3}\right)M_n=0. \qquad \text{(A.3)}
\end{aligned}
$$

A.4. Parasitic loop 3

$$
\begin{aligned}
&j\omega\left(\frac{L_C}{6}+\frac{L_{NC}}{2}+\frac{2M}{3}\right)I_n+j\omega\left(\frac{L_C}{3}+\frac{L_{NC}}{2}+\frac{M}{3}\right)I_{n+1}\\
&-j\omega\left(\frac{L_C}{6}+L_{NC}+\frac{2M}{3}\right)J_n\\
&-j\omega\left(\frac{L_C}{3}+L_{NC}+\frac{M}{3}\right)K_n\\
&-\left\{j\omega\left(\frac{L_C}{2}+L_{NC}\right)+\frac{16}{j\omega C_P}\right\}L_n\\
&-j\omega\left(\frac{L_C}{3}+L_{NC}+\frac{M}{3}\right)M_n=0. \qquad \text{(A.4)}
\end{aligned}
$$

A.5. Parasitic loop 4

$$
\begin{aligned}
&j\omega\left(\frac{L_{NC}}{2}+M\right)I_n+j\omega\left(\frac{L_C}{2}+\frac{L_{NC}}{2}\right)I_{n+1}\\
&-j\omega(L_{NC}+M)J_n\\
&-j\omega\left(\frac{L_C}{6}+L_{NC}+\frac{2M}{3}\right)K_n\\
&-j\omega\left(\frac{L_C}{3}+L_{NC}+\frac{M}{3}\right)L_n\\
&-\left\{j\omega\left(\frac{L_C}{2}+L_{NC}\right)+\frac{16}{j\omega C_P}\right\}M_n=0. \qquad \text{(A.5)}
\end{aligned}
$$

References

[1] Brillouin L 1946 *Wave Propagation in Periodic Structures: Electric Filters and Crystal Lattices* (New York: McGraw Hill)

[2] Matthaei G L, Young L and Jones E M T 1964 *Microwave Filters, Impedance Matching and Coupling Structures* (New York: McGraw Hill)

[3] Levy R and Cohn S B 1984 A history of microwave filter research, design and development *IEEE Trans. Microw. Theory Tech.* **32** 1055–67

[4] Spangenberg K R 1946 The universal characteristics of triple-resonant circuit bandpass filters *Proc. IRE* **34** 629–34

[5] Dishal M 1949 Design of dissipative band-pass filters producing desired exact amplitude-frequency characteristics *Proc. IRE* **37** 1030–51

[6] Cohn S B 1957 Direct-coupled-resonator filters *Proc. IRE* **45** 187–96

[7] Levy R 1967 Theory of direct-coupled cavity filters *IEEE Trans. Microw. Theory Tech.* **15** 340–8

[8] Hong J-S and Lancaster M J 1997 Theory and experiment of novel microstrip slow-wave open loop resonator filters *IEEE Trans. Microw. Theory Tech.* **45** 2358–65

[9] Shamonina E, Kalinin V A, Ringhofer K H and Solymar L 2002 Magnetoinductive waveguide *Electron. Lett.* **38** 371–3

[10] Wiltshire M C K, Shamonina E, Young I R and Solymar L 2003 Dispersion characteristics of magneto-inductive waves: comparison between theory and experiment *Electron. Lett.* **39** 215–7

[11] Shamonina E and Solymar L 2004 Magneto-inductive waves supported by metamaterial elements: components for a one-dimensional waveguide *J. Phys. D: Appl. Phys.* **37** 362–7

[12] Wiltshire M C K, Shamonina E, Young I R and Solymar L 2004 Experimental and theoretical study of magneto-inductive waves supported by one-dimensional arrays of 'swiss rolls' *J. Appl. Phys.* **95** 4488–93

[13] Shadrivov I V, Reznik A N and Kivshar Y S 2007 Magnetoinductive waves in arrays of split-ring resonators *Physica* B **394** 180–3

[14] Jylhä L, Maslovski S and Tretyakov S 2009 Traveling waves along the metasolenoid *Progress in Electromagnetics Research Symp. (Cambridge, MA, USA, 26–29 March 2009)*

[15] Liu H, Genov D A, Wu D M, Liu Y M, Steele J M, Sun C, Zhu S N and Zhang X 2006 Magnetic plasmon propagation along a chain of connected subwavelength resonators at infrared frequencies *Phys. Rev. Lett.* **97** 243902

[16] Stevens C J, Chan C W T, Stamatis K and Edwards D J 2010 Magnetic metamaterials as 1D data transfer channels: an application for magneto-inductive waves *IEEE Trans. Microw. Theory Tech.* **58** 1248–56

[17] Chan W T and Stevens C J 2011 Two-dimensional magneto-inductive wave data structures *Proc. 5th European Conf. on Antennas and Propagation (Rome, Italy, 11–15 April)* pp 1071–5
[18] Sun Z and Akyildiz I F 2010 Magnetic induction communications for wireless underground sensor networks *IEEE Trans. Antennas Propag.* **58** 2426–35
[19] Sun Z, Aykildiz I F and Kisseleff S 2013 Increasing the capacity of magnetic induction communications in challenged environments *IEEE Trans. Commun.* **61** 3943–52
[20] Agbinya J I and Masihpour M 2012 Power equations and capacity performance of magnetic induction communication systems *Wirel. Pers. Commun. J.* **64** 831–45
[21] Gulbahar B and Akan O B 2012 A communication theoretical modeling and analysis of underwater magneto-inductive wireless channels *IEEE Trans. Wirel. Commun.* **11** 3326–34
[22] Zhong W, Lee C K and Hui S Y R 2013 General analysis on the use of Tesla's resonators in domino forms for wireless power transfer *IEEE Trans. Ind. Electron.* **60** 261–70
[23] Puccetti G, Reggiani U and Sandrolini L 2013 Experimental analysis of wireless power transmission with spiral resonators *Energies* **6** 5887–96
[24] Puccetti G, Stevens C J, Reggiani U and Sandrolino L 2015 Experimental and numerical investigation of termination impedance effects in wireless power transfer via metamaterial *Energies* **8** 1882–95
[25] Stevens C J 2015 A magneto-inductive wave wireless power transfer device *Wirel. Power Transfer* **2** 51–9
[26] Agbinya J I 2013 A magneto-inductive link budget for wireless power transfer and inductive communications *Prog. Electromagn. Res.* C **37** 15–28
[27] Chen Y, Munukutla S, Pasupathy P, Neikirk D P and Wood S L 2010 Magneto-inductive waveguide as a passive wireless sensor net for structural health monitoring *Proc. SPIE* **7647** 764749
[28] Floume T 2011 Magneto-inductive conductivity sensor *Metamaterials* **5** 206–17
[29] Freire M J and Marques R 2005 Planar magnetoinductive lens for three-dimensional subwavelength imaging *Appl. Phys. Lett.* **86** 182505
[30] Freire M J and Marques R 2006 Near-field imaging in the megahertz range by strongly coupled magnetoinductive surfaces: experiment and *ab initio* analysis *J. Appl. Phys.* **100** 063105
[31] Lapine M, Jelinek L, Marqués R and Freire M J 2010 Exact modelling method for discrete finite metamaterial lens *IET Microw. Antennas Propag.* **4** 1132–9
[32] Syms R R A, Floume T, Young I R, Solymar L and Rea M 2010 Flexible magnetoinductive ring MRI detector: design for invariant nearest neighbour coupling *Metamaterials* **4** 1–14
[33] Syms R R A, Young I R, Ahmad M M and Rea M 2012 Magnetic resonance imaging with linear magneto-inductive waveguides *J. Appl. Phys.* **112** 114911
[34] Syms R R A, Young I R, Solymar L and Floume T 2010 Thin-film magneto-inductive cables *J. Phys. D: Appl. Phys.* **43** 055102
[35] Syms R R A, Solymar L and Young I R 2010 Broadband coupling transducers for magneto-inductive cables *J. Phys. D: Appl. Phys.* **43** 285003
[36] Syms R R A and Solymar L 2010 Bends in magneto-inductive waveguides *Metamaterials* **4** 161–9
[37] Lomanets V, Zhuromskyy O, Onishchukov G and Peschel U 2012 Electrical circuit model of arrays of resonant elements *Phys. Rev.* B **85** 125110
[38] Hesmer F, Tatartschuk E, Zhuromskyy O, Radkovskaya A A, Shamonin M, Hao T, Stevens C J, Faulkner G, Edwards D J and Shamonina E 2007 Coupling mechanisms for split ring resonators: theory and experiment *Phys. Status Solidi* b **2044** 1170–5
[39] Radkovskaya A, Sydoruk O, Tatartschuk E, Gneiding N, Stevens C J, Edwards D J and Shamonina E 2011 Dimer and polymer metamaterials with alternating electric and magnetic coupling *Phys. Rev.* B **84** 125121
[40] Syms R R A and Floume T 2013 Electric coupling in strongly coupled magneto-inductive cable *7th Int. Congress on Advanced Electromagnetic Metamaterials in Microwaves and Optics (Bordeaux, France, 16–21 September 2013)*